Electronic Supplementary Information for

Manganous Oxide Nanoparticles Encapsulated in Few-layer Carbon as an efficient electrocatalyst for Oxygen Reduction in alkaline media

Han Cheng,[‡a] Kun Xu,[‡a] Lili Xing,[b] Si Liu,[a] Yue Gong,[c] Lin Gu,[c] Lidong Zhang[b] and Changzheng Wu*[a]

[a]Hefei National Laboratory for Physical Science at Microscale, iChEM (Collaborative Innovation Center of Chemistry for Energy Materials), Hefei Science Center (CAS) and CAS Key Laboratory of Mechanical Behavior and Design of Materials, University of Science and Technology of China, Hefei, Anhui 230026 (P. R. China), E-mail: czwu@ustc.edu.cn

[b] National Synchrotron Radiation Laboratory, University of Science and Technology of China, Hefei, Anhui 230026 (P. R. China)

[c] Beijing National Laboratory for Condensed Matter Physics, Collaborative Innovation Center of Quantum Mater and Institute of Physics, Chinese Academy of Sciences, Beijing100190 (P. R. China)

[‡]These authors contributed equally to this work

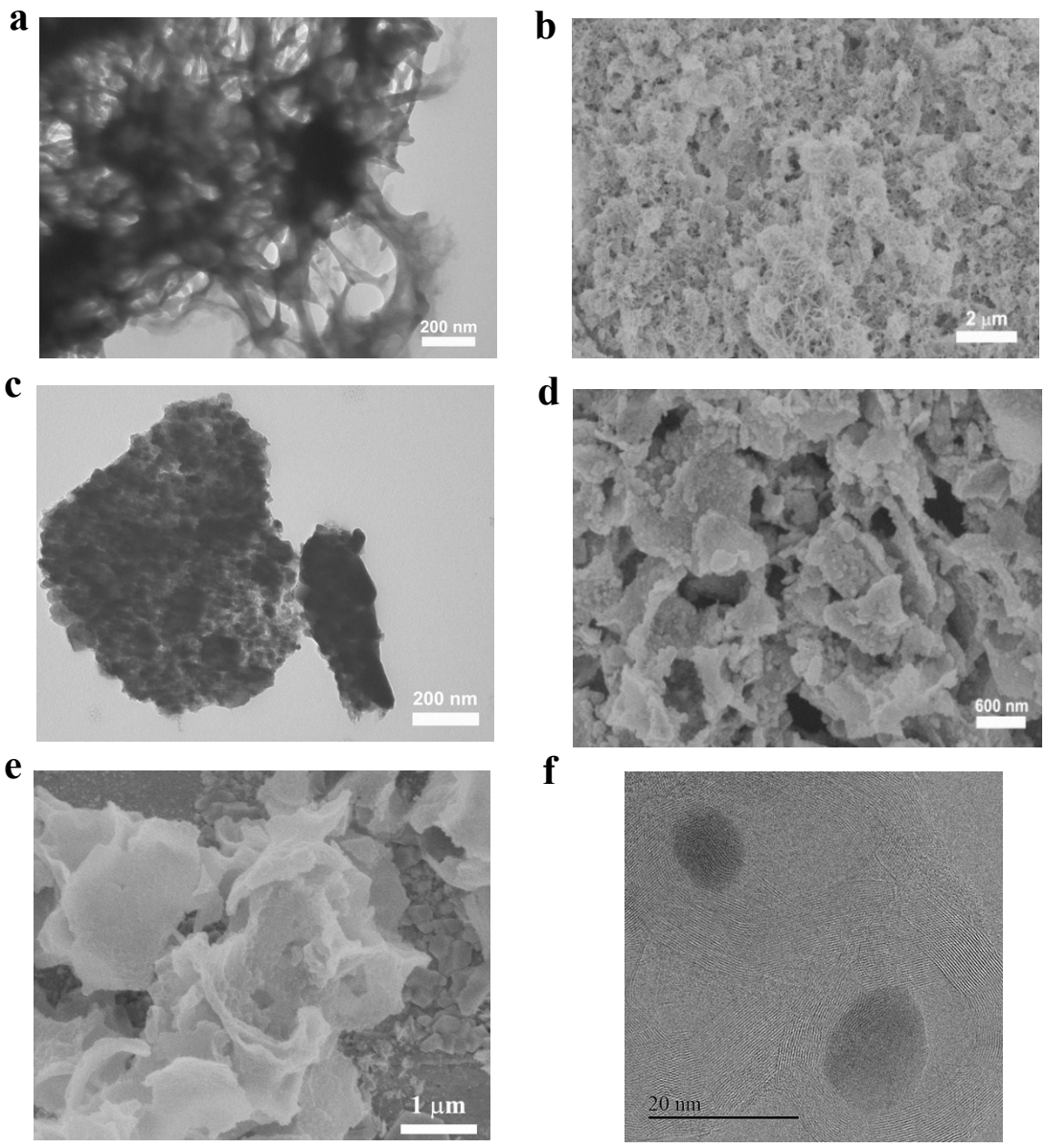

Figure S1. (a) TEM and (b) SEM images of precursor $C_4H_4MnO_5$•$3H_2O$. (c) TEM and (d) SEM images of precursor after the first pyrolysis at 800℃. (e) SEM images of prepared MnO@FLC which was after acid etching and twice pyrolysis. (f) HRTEM image of as-prepared MnO@FLC.

The $C_4H_4MnO_5 \cdot 3H_2O$ precursors exhibit a wire-like morphology (Figure S1a) and several micrometers interlinked with each other to form a fibrous network. The Figure S1c shows that the Mn-containing particles were encapsulated in carbon layers after the first pyrolysis at 800℃. The diluted hydrochloric was used to remove non-activated sites of Mn and the second pyrolysis follows.

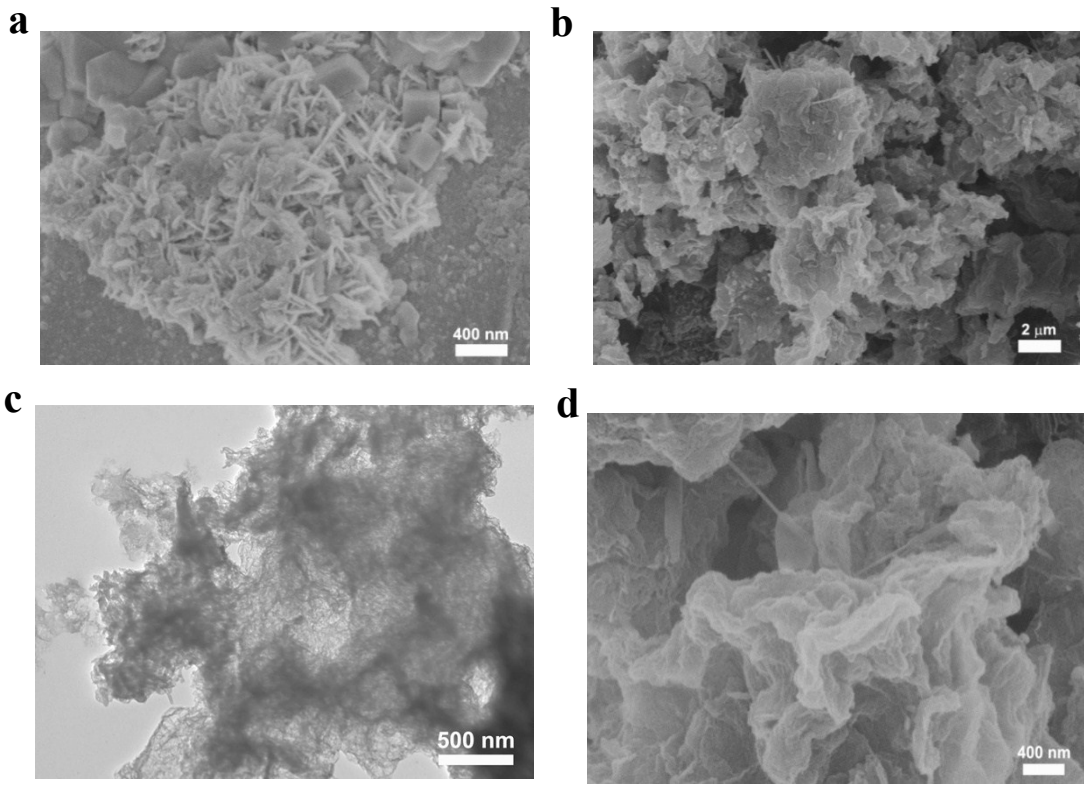

Figure S2. (a) SEM images of precursor $C_4H_5NaO_5$. (b) SEM images of precursor after the first pyrolysis at 800℃. (c) TEM and (d) SEM images of control sample SdMC which was after acid etching and twice pyrolysis.

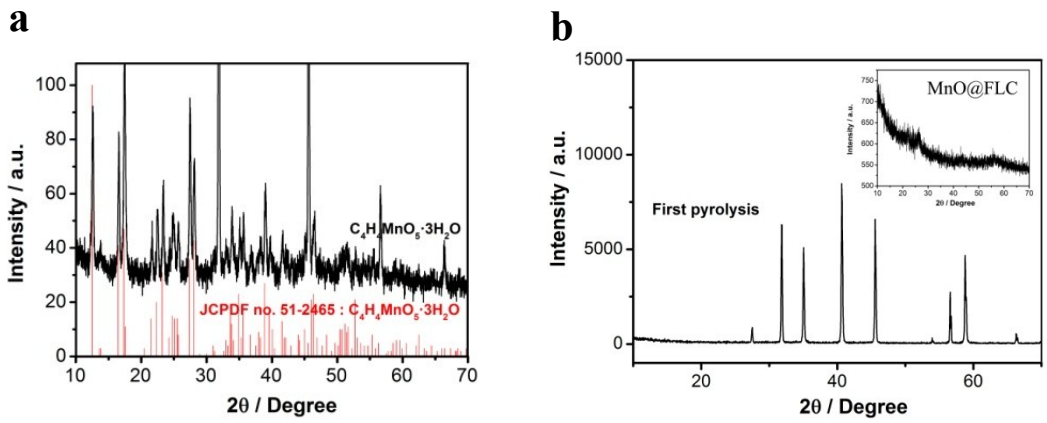

Figure S3. (a) XRD patterns of precursor $C_4H_4MnO_5 \cdot 3H_2O$ as prepared product (black) and reference (red). (b) XRD pattern after the first pyrolysis and prepared MnO@FLC (inset).

The X-ray diffraction (XRD) patterns also support the successful synthesis of MnO@FLC. The pattern peaks (Figure S3a) of malate trihydrate ($C_4H_4MnO_5 \bullet 3H_2O$) precursors match the reference sample (JCPDF Card no.51-2465) in principle. The lattice parameters were refined to orthorhombic phase of a = 14.211 Å, b = 8.278 Å and c = 14.692 Å in Pbca space group. Then the first pyrolysis at 800℃ conducts and the XRD patterns (Figure S3b) indicate the mixture of $C_4H_4MnO_5 \cdot 3H_2O$ and MnO. The MnO (JCPDF Card No.78-0424) lattice parameters are calculated to be $a = b = c$ = 4.445 Å in an Fm-3m space group.

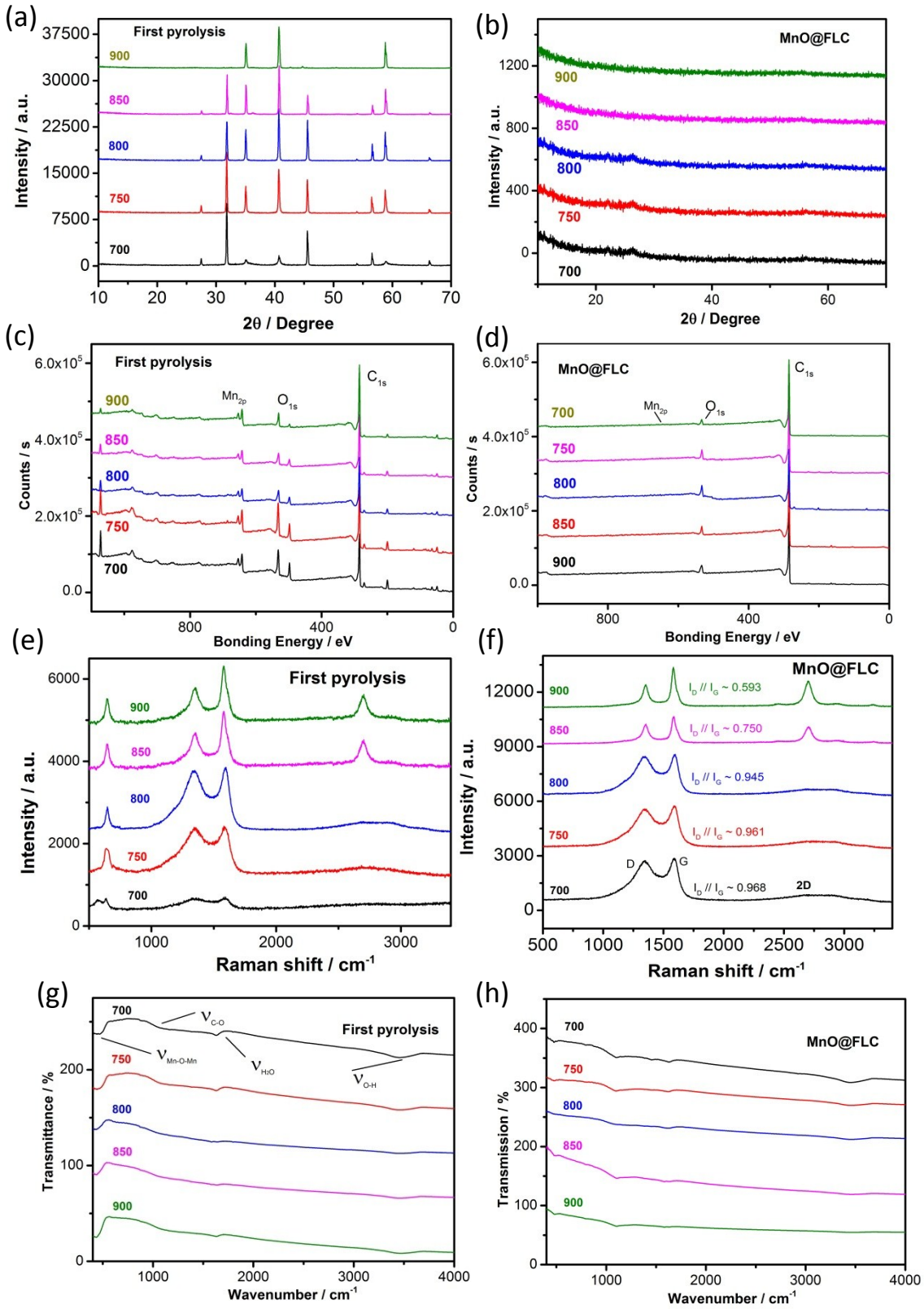

Figure S4. XRD patterns of precursor after the first pyrolysis (a) and MnO@FLC (b) at different temperatures. XPS data of sample after the first pyrolysis (c) and MnO@FLC (d). Raman spectra of sample after the first pyrolysis (e) and MnO@FLC (f). FTIR of sample after the first pyrolysis (g) and MnO@FLC (h).

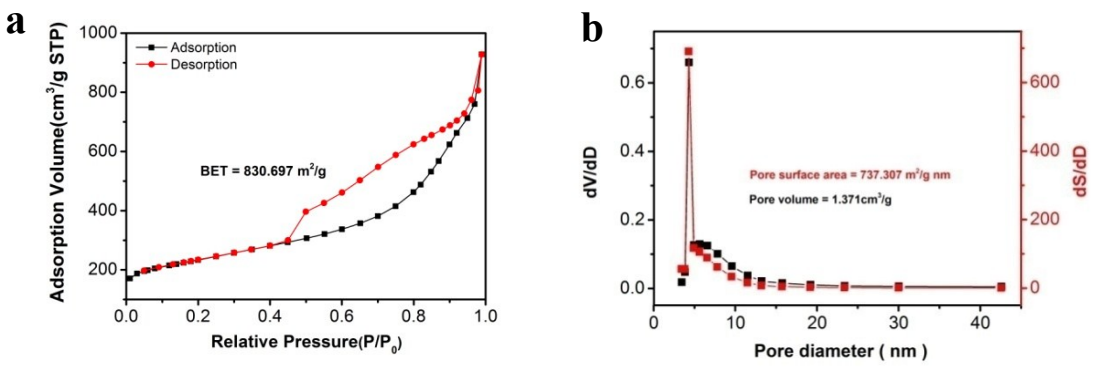

Figure S5. (a) Nitrogen adsorption and desorption isotherm plots of MnO@FLC catalysts. (b) Barrett–Joyner–Halenda pore size distribution of the MnO@FLC.

Nitrogen sorption analysis of MnO@FLC gave evidence for a high Brunauer–Emmett–Teller (BET) surface area of 830.697 $m^2 g^{-1}$. Well-defined mesopores with size of ~5nm are obtained for such frameworks, with a pore volume of ~1.371 $cm^3 g^{-1}$ and surface of 737 $m^2 g^{-1}$. These results demonstrate the successful fabrication of the porous frameworks outside the few-layer carbon active sites. It can be speculated that the porous carbon is synthesized by acid washing of non-active MnO nanoparticles. This porous structure provides high specific surface areas for ORR activity and it also offer pathway for oxygen species transport.

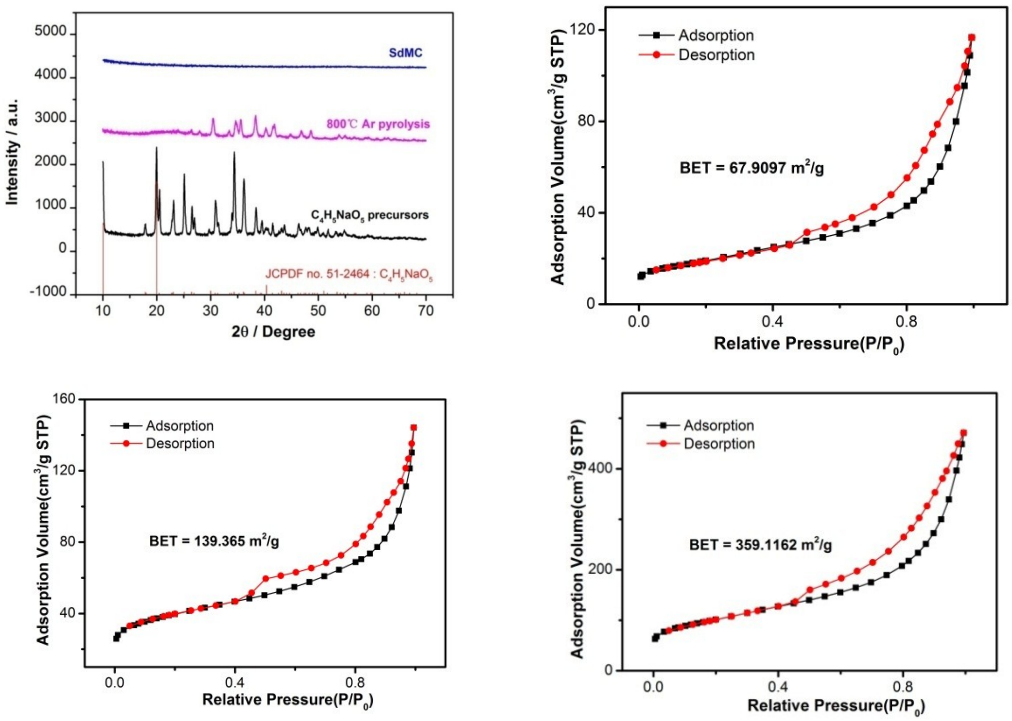

Figure S6. (a) XRD patterns of precursor $C_4H_5NaO_5$ control sample (black) and precursor after the first pyrolysis at 800℃ (purplish red) and control sample SdMC (blue). Nitrogen adsorption and desorption isotherm plots of precursor $C_4H_5NaO_5$ sample (b)、first pyrolysis (c) and SdMC (d).

The X-ray diffraction (XRD) patterns support the formation of sodium malate trihydrate $C_4H_5NaO_5$ (Figure S6) and the peaks match the reference sample (JCPDF Card no.51-2464) in principle. The lattice parameters were refined to monoclinic phase of a = 10.096 Å, b = 6.05 Å and c = 10.356 Å in Pa space group.

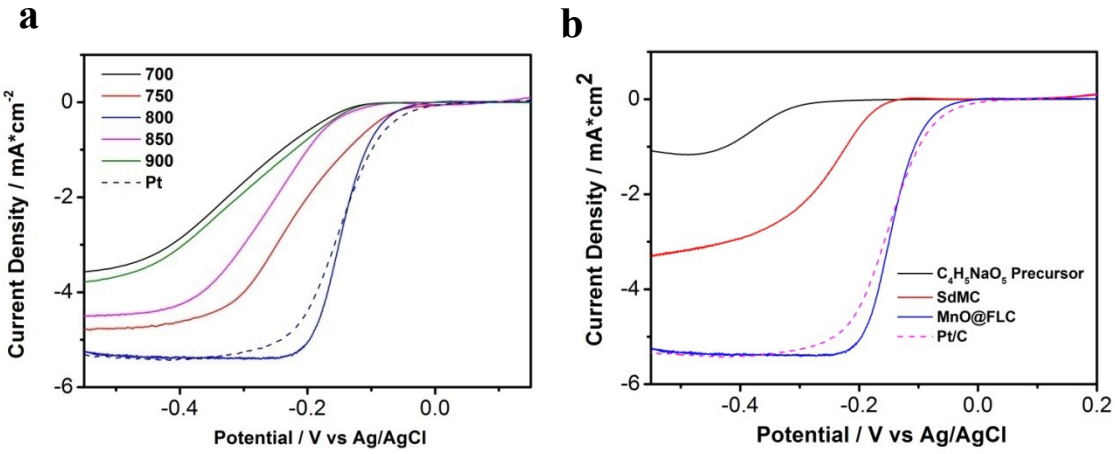

Figure S7. (a) ORR activity of MnO@FLC at different temperatures. (b) ORR activity of $C_4H_5NaO_5$ precursor (black)、control sample SdMC (red).

To find an optimum pyrolysis temperature of this manganese malate derived porous carbon, the ORR activity of MnO@FLC is shown in Figure S7a. The results confirm the best ORR activity in alkaline condition is the MnO@FLC pyrolyzed at 800℃. The ORR activity has improved greatly. The function of MnO nanoparticles was also investigated by comparing the ORR activity in MnO@FLC with the sodium malate derived porous carbon (SdMC) control sample which does not contain MnO nanoparticles. The synthesis method of SdMC is similar to the procedure of MnO@FLC except for the addition of manganese resource ($MnCl_2 \cdot H_2O$). We could observe a quite low ORR activity of SdMC and it indicated that the MnO nanoparticles play an important role in ORR active sites.

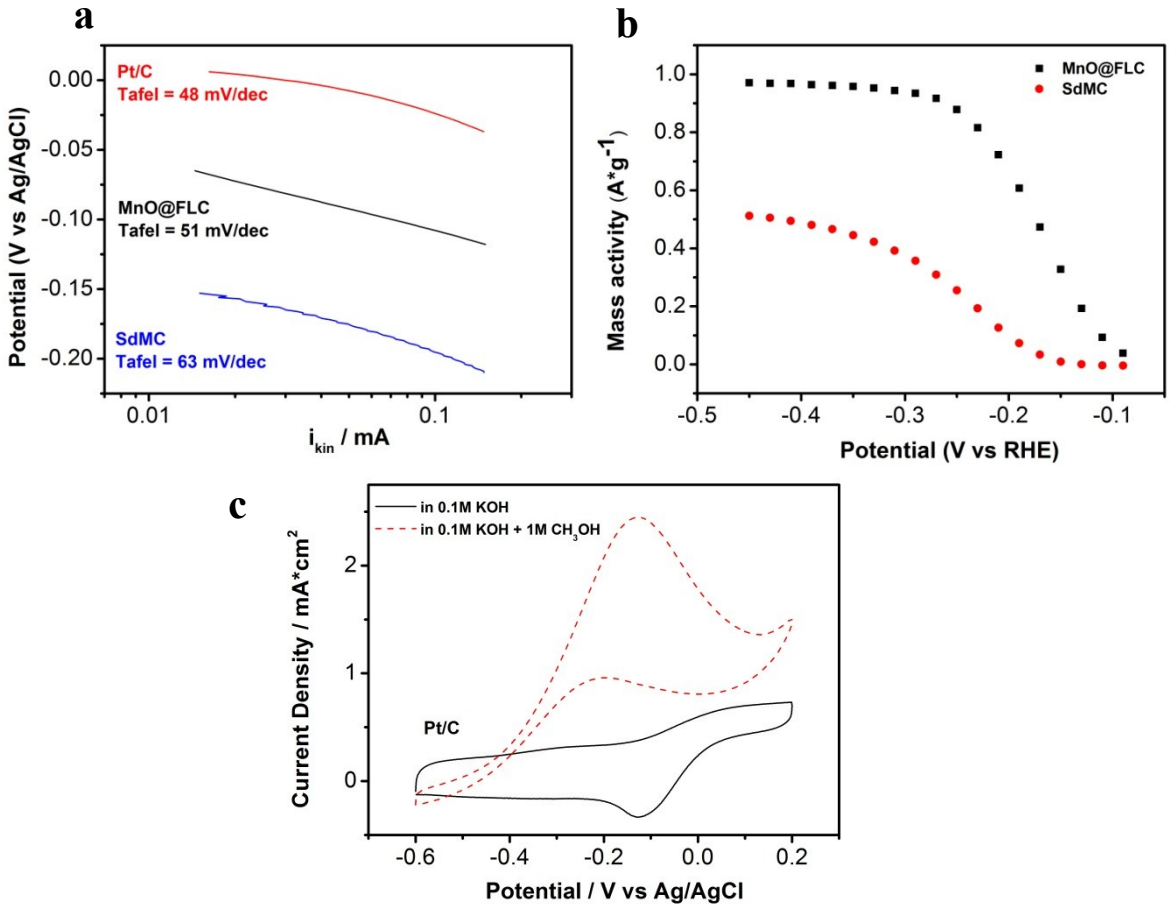

Figure S8. (a) Tafel slope of MnO@FLC, SdMC and Pt/C. (b) Mass activity of MnO@FLC and SdMC. (c) Pt/C catalysts before (black) and after (red) adding 1 M CH_3OH in O_2-saturated 0.1M KOH.

To understand the further mechanism of ORR procedure in MnO@FLC and Pt/C catalysts, the Tafel slope analysis was shown in Figure S8a. MnO@FLC has the similar Tafel slope with the Pt/C catalysts while the SdMC is higher. It indicated that the $4e^-$ transformation process during ORR which was catalyzed by MnO@FLC.

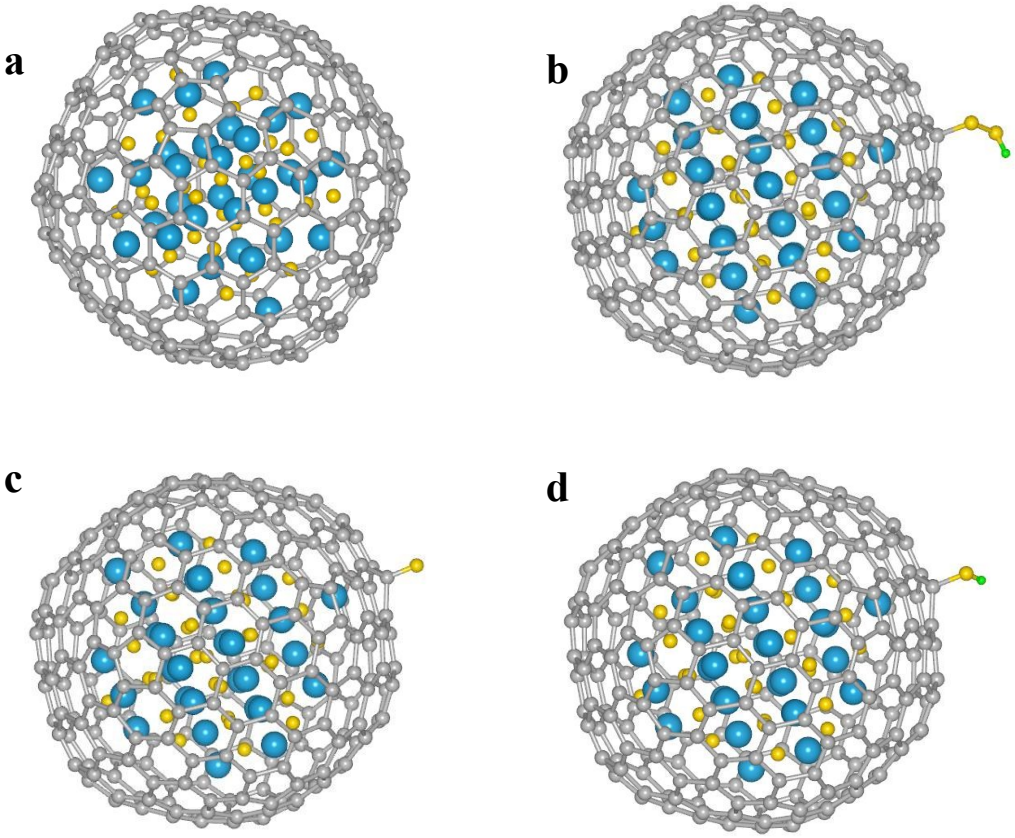

Figure S9. Model of MnO@FLC (a) bonding with *OOH (b), *O (c) and *OH (d). Colors: Mn blue, O yellow, C grey, H green.

The VASP model is a 25 Å× 25 Å× 25 Å lattice, within which the C240 fullerene and MnO crystal fits inside. In order to ensure all the atoms sitting at the energy minimum point while for static calculation, all structures were fully relaxed for geometry optimization. For each step, the reaction free energy ΔG is described as the difference between free energies of the initial and final states and is calculated in this work by the widely used method in previous studies.[9-11]

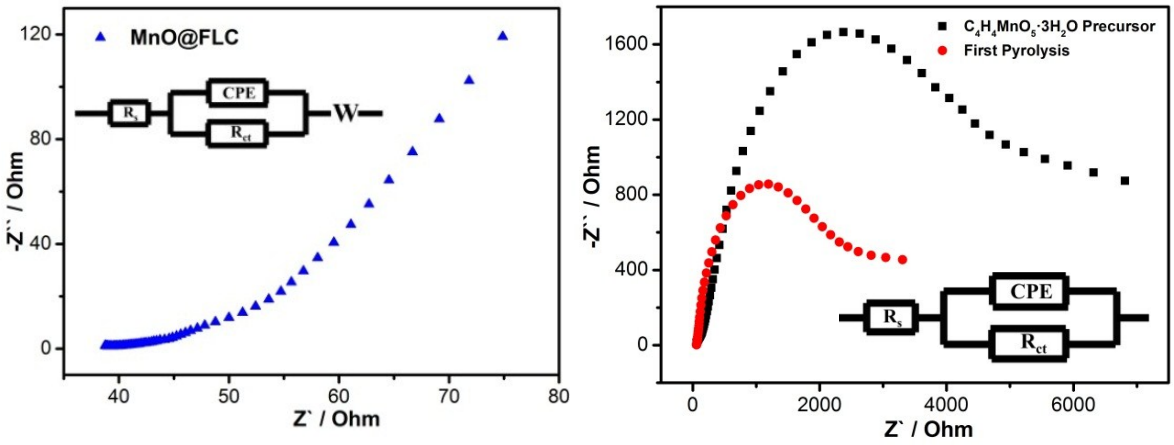

Figure S10. EIS results with equivalent circuit of MnO@FLC (blue) and the precursors and the first pyrolysis sample from 10 KHz to 0.01 Hz in the mixed diffusion-controlled region of MnO@FLC. An ac sinusoidal perturbation of 5 mV in amplitude was superimposed on a dc bias.

The curves of MnO@FLC sample show a little bend at about 47 Ohm (Z`), which correspond to the charge transfer resistance. Then 45 degree angle of straight line occurs, which represents the Warburg resistance. The charge transfer resistance is much less than and covered by Warburg resistance (Rct<<W). By comparison, we can see a great difference in precursors and the first pyrolysis sample. We can see a large charge transfer resistance in precursors and the first pyrolysis sample without the observation of the Warburg resistance. This illustrates the inactive catalytic performance of the precursors and the MnO@FLC sample is significantly superior to the precursors.

Table S1. Element compositions of MnO@FLC catalysts pyrolyzed at different temperatures determined by ICP-OES

ICP-OES					
Temperature	700	750	800	850	900
Mn (μg/g)	1777	1315.4	994.6	748.2	233.9

Table S2. The performance comparisons of different manganese oxide composites for ORR in terms of onset potential, half-wave potential and limiting current density (mA cm^{-2}).

Catalysts	Onset Potential (V) vs Ag/AgCl	Half-wave potential (V) vs Ag/AgCl	Limiting current density (mA cm-2)	Ref.
MnO@FLC	-0.0052	-0.1531	-5.38	This work
MnO_2/CNT	-0.3024	-0.4153	-2.4	[1]
1.0 wt.%Pt@MnO_2	-0.2362	-0.312	-1.25	[2]
long belt like a-MnO2	-0.032	-0.264	-4.4	[3]
a-MnOx on KB	-0.0192	-0.159	-4.41	[1]
Hierarchical MnO_2 rGO	-0.286	-0.294	-4.3	[4]
MnOx–CeO2/KB hybrid	-0.012	-0.154	-5.2	[5]
Layered MnO_2 nanosheets	-0.154	-0.248	-2.3	[6]
MnOx/C	0	-0.134	-3.2	[7]
Ni–MnOx/C	0.005	-0.129	6.7	[8]
Pt/C	0.0098	-0.1489	-5.36	/

Reference

1 C. W. Woon, H. R. Ong, K. F. Chong, K. M. Chan, M. M. R. Khan, *Procedia Chemistry* 2015, **16**, 640..

2 X. Wu, X. Gao, L. Xu, T. Huang, J. Yu, C. Wen, Z. Chen, J. Han, Int. J. Hydrogen. Energ. (doi:10.1016/j.ijhydene.2016.04.216).

3 Y. Ma, R. Wang, H. Wang, J. Key, S. Ji, *J. Power. Sources* 2015, **280**, 526.

4 D. Guo, S. Dou, X. Li, J. Xu, S. Wang, L. Lai, H. K. Liu, J. Ma, S. X. Dou, *Int. J. Hydrogen. Energ*. 2016, **41**, 5260.

5 C.-H. Kuo, I. M. Mosa, S. Thanneeru, V. Sharma, L. Zhang, S. Biswas, M. Aindow, S. P. Alpay, J. F. Rusling, S. L. Suib, *Chem. Commun.* 2015, **51**, 5951.

6 C. Shi, G.-L. Zang, Z. Zhang, G.-P. Sheng, Y.-X. Huang, G.-X. Zhao, X.-K. Wang, H.-Q. Yu, *Electrochimica Acta*. 2014, **13**, 2239.

7 I. Roche, E. Chaînet, M. Chatenet, J. Vondrák, *J. Phy. Chem. C* 2007, **111**, 1434.

8 I. Roche, E. Chaînet, M. Chatenet, J. Vondrák, *J. Appl. Electrochem.* 2008, **38**, 1195.

9 S. Zuluaga, S. Stolbov, *J. Chem. Phys.* 2011, **135**, 134702.

10 I. C. Man, H. Y. Su, F. Calle-Vallejo, H. A. Hansen, J. I. Martínez, N. G. Inoglu, J. Kitchin, T. F. Jaramillo, J. K. Nørskov, J. Rossmeisl, *ChemCatChem*, 2011, **3**, 1159.

11 J. K. Nørskov, J. Rossmeisl, A. Logadottir, L. Lindqvist, J. R. Kitchin, T. Bligaard, H. Jonsson, *Phys. Rev. B*, 2004, **108**, 17886.